Spatio-temporal features of ionospheric disturbances resulting from March 2023 geomagnetic storm: Comparisons with March 2015 St. Patrick's Day storm

Waqar Younas, Majid Khan, C. Amory-Mazaudier, Yukitoshi Nishimura, M. Kamran

Spatio-Temporal Features of Ionospheric Disturbances Resulting from March 2023 Geomagnetic Storm: Comparisons with March 2015 St. Patrick's Day Storm

Waqar Younas[1,2,3], Majid Khan[3], C. Amory-Mazaudier[4], Yukitoshi Nishimura[1] and M. Kamran[5]

[1]Center for Space Physics, Boston University, Boston, MA, USA

[2]Cooperative Programs for the Advancement of Earth System Science (CPAESS), University Corporation for Atmospheric Research, Boulder, CO, USA

[3]Department of Physics, Quaid-i-Azam University Islamabad 45320, Pakistan

[4]Sorbonne Université, Ecole polytechnique, Institut Polytechnique de Paris, Université Paris Saclay, Observatoire de Paris, CNRS, Laboratoire de Physique des Plasmas (LPP), 75005 Paris, France

[5]Department of Physics, COMSATS University Islamabad, Park Road Chak Chehzad, Islamabad, Pakistan

Corresponding author: Majid Khan (Majid.Khan@qau.edu.pk)

Highlights

- There is no positive storm effect observed in the Pacific mid-latitude regions during the March 2023 storm.
- Hemispheric asymmetry is observed in the super-fountain effect during the March-23 storm.
- The storm-induced disturbed thermospheric winds display a non-uniform planetary distribution, which is particularly evident during the March-23 storm.

Keywords

Geomagnetic storm; ionospheric variations; ionospheric disturbance; global ionospheric maps

58

59

60

Abstract

This study explores the ionospheric disturbances induced by the March 2023 geomagnetic storm, offering insights into the complex interplay between space weather events and the Earth's upper atmosphere. In this regard, data from ionospheric maps (global and regional electron contents) and topside plasma density (provided by the Swarm satellites) have been used. Furthermore, the findings are compared with those of the March 2015 St. Patrick's Day storm of solar cycle 24, which exhibited notably similar onset conditions. The Global Electron Content (GEC) displays substantial positive surges in the African, Pacific, and American sectors, with a notable enhancement in the American sector on March 24, 2023. During the recovery phase (March-23 storm), negative storm effects are observed across all longitudinal sectors, with greater intensity at low-latitudes compared to mid-latitudes. Moreover, the study highlights discrepancies in positive storm effects when compared to the St. Patrick's Day storm. During the March-2023, there was no positive storm effect observed in the pacific mid-latitude regions. This longitudinal difference in occurrence of positive storm may be attributed to potential influences from variations in the z-component of the interplanetary magnetic field and energy inputs into the magnetosphere. A super fountain effect is observed exclusively in the American sectors during both storms, exhibiting a noticeable hemispheric asymmetry. The non-uniform planetary distribution of disturbed thermospheric winds likely played a major role in the ionospheric asymmetry in the American region during the 2023 event.

1. Introduction

Understanding the intricate dynamics of ionospheric disturbances remains one of the formidable challenges for researchers engaged in the exploration of the upper atmosphere (Heelis & Maute, 2020). The identification of source mechanisms behind these disturbances within the ionosphere-thermosphere system poses substantial challenges, hindering the effective modeling of the system during geomagnetic storms (Unnikrishnan et al., 2006 Ogunsua et al., 2014; Materassi et al., 2023). The elusive nature of these physical mechanisms has, in turn, impeded our ability to predict and mitigate the potential impacts on essential technologies that depend on stable ionospheric conditions. The geomagnetic storms can introduce a distinct set of conditions, leading to a variable ionospheric response in each instance. In this regard, several factors contribute to the complex nature of ionospheric response, e.g., time of storm commencement, the specific season during which the storm takes place, the origin of Coronal Mass Ejections (CMEs), and the orientation of the z-component of the interplanetary magnetic field (IMF) (Tsurutani et al., 2004, Balan et al., 2009, Koga et al., 2009; Liu et al., 2019).

The present study is dedicated to unraveling the ionospheric response to the geomagnetic event of March 23rd, 2023, hereafter referred to as the March-23 storm. Using data from ground-based and satellite instruments, we aim to address some of the complexities of ionospheric modifications as caused by the specific coronal hole activity under examination. Nava et al. (2016) conducted a thorough investigation of the St. Patrick's Day storm of 2015 (referred as the March-15 in our study). This storm, considered as the most intense event of solar cycle 24, was analyzed at both low and mid-latitudes using ground-based as well as satellite-based observations. They reported longitudinal disparities in ionospheric variations by categorizing them into four regions, namely Asia,

Africa, America, and the Pacific. Moreover, effects of prompt penetration (and disturbance dynamo) electric fields have been highlighted using the spectral analysis of magnetic data. Astafyeva et al. (2015) also investigated the March-15 storm, using global multi-instrument analysis, and reported a significant positive ionospheric storm at low-latitudes in the morning and post sunset sectors (mostly located in the eastern pacific region). Such enhancements during storm periods were primarily attributed to the increase in thermospheric O/N_2. Due to the significant impact of the March-15 storm, several authors have extensively investigated it from various perspectives (Wu et al., 2016; Maurya et al., 2018; Mridula et al., 2022).

Notably, the March-23 storm exhibits compelling similarities with the March-15 counterpart. This interesting parallelism presents an opportunity to gain insights into the underlying physical processes that can influence the spatio-temporal variations of ionospheric disturbances during the geomagnetic storms and is the main topic of present study. By drawing connections between these distinct but analogous events, we endeavor to enhance our understanding of the multifaceted nature of ionospheric responses to solar-terrestrial interactions. This study aims to characterize the temporal and spatial patterns of ionospheric disturbances during the March 2023 geomagnetic storm, focusing on both positive and negative storm effects across different longitude sectors. We have examined the influence of key drivers, such as penetration electric fields and thermospheric winds, in shaping these ionospheric responses. Furthermore, this work investigates potential hemispheric asymmetry in the equatorial ionization anomaly (EIA) by analyzing TEC variations between the northern and southern crests. By comparing the March 2023 storm with the St. Patrick's Day storm, we seek to understand the role of various global parameters in driving ionospheric disturbances.

The subsequent sections of this work are structured to provide a comprehensive overview. Section 2 details the datasets employed, and the methodology applied in analyzing the ionospheric changes associated with the considered coronal hole activity. The results are presented in Section 3, followed by a discussion in Section 4. In conclusion, we summarize our findings and their implications in Section 5, offering a perspective on the ionospheric disturbances as observed during the March-23 storm and their potential implications for space weather forecasting and technology resilience.

2. Data Sets and Methodology

Our investigations of the ionospheric variations involve the use of diverse datasets and methodologies, each serving specific purposes. The following list provides a brief overview of the parameters and their corresponding indices.

a) Relevant solar wind parameters and various geomagnetic activity indices have been obtained from the OMNIWeb data center, which is accessible at http://omniweb.gsfc.nasa.gov/.
b) World data center (WDC) for geomagnetism (https://wdc.kugi.kyoto-u.ac.jp) provides the AE index, which is a key index to estimate the energy input to ionosphere. Since provisional AE index was not available for March 2023 storm, we reproduced it from the online quick-look plots created on 05 Jan 2023 (https://wdc.kugi.kyoto-u.ac.jp/ae_realtime/index.html).
c) Calculations for the Global Electron Content (GEC) and Regional Electron Content (REC) were performed using global ionospheric maps as provided by UPC-UQRG (Afraimovich et al., 2006; Nava et al., 2016; Younas et al., 2020). The hemispheric REC is computed by dividing the GEC into four longitudinal bands, i.e. (60:150E), (-30:60E), (-120:-30E) , (-120:-180E, 150:180E) corresponding to Asia, Africa, America and Pacific, respectively. Furthermore, low- and mid-latitudes REC are also computed by restricting the latitude in each hemisphere to the range (0:30) and (30:60), orderly.
d) Variations in topside ionospheric plasma density (N_e) were deduced from measurements obtained by the SWARM satellites, namely SWARM A, B, and C (Olsen et al., 2013). During the period from March 22 to 25, 2023, SWARMs A and C traversed the equator at approximately 20.3 LT (ascending) and 8.3 LT (descending), respectively, while SWARM B accomplished this around 10.5 LT (ascending) and 22.3 LT (descending). It is noteworthy that, due to their synchronous orbits, SWARMs A and C exhibit comparable N_e values. For brevity, only results from SWARM A are presented herein.
e) Thermospheric O/N2 composition changes as measured by the global ultraviolet imager (GUVI) on board the thermosphere, ionosphere, mesosphere energetics and dynamics (TIMED) satellite have been considered in this work.

3. Results

On March 20, 2023, the AIA-193 instrument on board the Solar Dynamics Observatory (SDO) observed a large coronal hole in the Sun's atmosphere. The associated high-speed solar wind was expected to reach Earth between March 23 and 24, 2023 (source: https://spaceweather.com).

Consequently, a CME struck the Earth on March 23 around 05:00 UT, as reported by Richardson and Cane. A prolonged southward-directed IMF-Bz led to a severe geomagnetic storm. In the following subsection, we will discuss the variations in different global parameters during this event.

3.1 Solar wind and geomagnetic activity parameters

Figure 1 depicts the global parameters in chronological order, encompassing the z-component of the interplanetary magnetic field (IMF-Bz), solar wind speed, solar wind pressure, auroral electrojet (AE) and the SYM-H index. The temporal scope of the illustration spans from March 21-23, 2023. The vertical dotted line indicates the beginning of geomagnetic activity on March 23rd at 06:00 UT.

The IMF-Bz exhibited a southward turn, briefly deviating northward at 13:00 UT before settling into a sustained southward orientation until 08:30 UT of the subsequent day. The lowest value of IMF-Bz, registering at -18.44 nT, manifested at 19:30 UT.

It is noteworthy that there were no substantial variations in solar wind speed following the CME event. However, solar wind pressure experienced an escalation, culminating at 22.2 nPa at 14:34 UT on the storm day. The AE index revealed several periods of energy input after the arrival of CME. The first enhancement in AE index started at 07:20 UT and reached to a maximum value of 1310 nT at 1113 UT. Another phase of AE enhancement began at 1720 UT and continued until the end of March 24th, with the maximum value (2610 nT) occurring at 2100 UT on March 23rd. The next significant peak in the AE index, reaching 1910 nT, occurred at 0700 UT on March 24th. Following the impact of the CME, the SYM-H index, a crucial metric for measuring ring current intensity, decreased, reaching a minimum value of -170 nT at 05:21 UT.

3.2 Global and regional electron content variations

In Figure 2 (top panel), the disparity in global electron content (ΔGEC) – calculated by subtracting the corresponding quiet time values from the period spanning March 21st to March 30th, 2023 – is illustrated. Notably, two distinct episodes of GEC enhancements emerge, peaking at 0.30 GECU and 0.41 GECU on March 23rd at 14:00 UT and 23:45 UT, respectively. These trends correspond to two episodes of energy input into the ionosphere, as indicated by the AE index (see Fig. 1, fourth panel) (Nava et al., 2016). Subsequently, GEC experiences a decline, exhibiting a minimum value of -0.46 GECU on March 24th at 13:15 UT. To delve deeper into the geographical distribution of these enhancements, we conducted an analysis of REC in four longitudinal sectors, namely Asia, Africa, America, and the Pacific (Figure 2, bottom panel). Following the initial GEC peak, an increase in the

REC is noted in Africa, while the subsequent peak is more prominent in the America and Pacific regions. The amplitude of the negative storm, indicative of a decrease in electron content, is most pronounced, on the following day of storm, in Asia (-0.30 GECU at 11:45 UT), followed by Africa (-0.19 GECU at 13:30 UT) and America (-0.17 GECU at 19:15 UT), respectively.

Furthermore, to assess the contribution of the low- and mid-latitude regions to the observed storm effects, we conducted an analysis of REC in the four longitudinal sectors of each hemisphere, as illustrated in Figure 3. The top left and right panels in Figure 3 represent the low-latitude REC of the northern and southern hemispheres, respectively. Notably, the low-latitude region in Asia exhibits no discernible positive storm effect but demonstrates a significant negative effect with nearly equal magnitude (-0.1 GECU) in both hemispheres. Positive storm effects exhibit similar characteristics in both hemispheres, with the maximum impact observed in the American low-latitude region, followed by the Pacific and Africa, respectively.

Conversely, the bottom left and right panels in Figure 3 depict a similar analysis for mid-latitude regions. The northern mid-latitude REC reveals a positive storm effect only in the African sector, reaching a maximum magnitude of 0.06 GECU. In the southern hemisphere, the positive storm effect is first observed in Africa, followed by the America and Pacific regions, respectively. However, the intensity of the positive enhancement at the southern mid-latitude region is highest for America, followed by the Pacific and Africa regions. The negative storm effect reaches its maximum for the mid-latitude regions of Asia and Africa, orderly for the northern and southern hemispheres.

3.3 ΔvTEC variations

Figure 4a illustrates the variations in ΔvTEC (Vertical Total Electron Content) in the eastern hemisphere at fixed longitudes, specifically 180°, 135°, 90°, and 45° from top to bottom. Several features can be discerned from these plots, e.g. on the storm day (23rd March), no significant disturbances are detected at any of the considered longitudes except at 180° where an enhancement is observable at the end of day. However, a pronounced negative storm effect is evident on 24th March, with the maximum intensity of ionospheric TEC depletion occurring in the 90° sector, followed, respectively by 135° and 45° counterparts. Conversely, this effect is notably weak in the 180° sector. The negative storm effect first appears in mid-latitudes and then propagates towards the equator. The most significant decrement, reaching -80 TECU, is observed at 90° longitude and 25° latitude. On March 25th and 26th, an enhancement in Total Electron Content (TEC) is observed in the crests of the Equatorial Ionization Anomaly (EIA), mainly in the

longitudes of 180° and 135°. Figure 4b mirrors the structure of 4a but focuses on the western hemisphere. In contrast to its eastern counterpart, no substantial negative storm effect is observed in this hemisphere. However, on 24th March, a robust positive storm is evident in the low and mid-latitudes. This increase in ionospheric TEC is more pronounced in the southern hemispheric regions. Notably, this enhancement remains observable at -135° and -180° longitude sectors in the crests of the EIA until the 25th and 26th of March 2023, orderly.

3.4 Topside ionospheric plasma density variations

The left and right columns in Figure 5 present the ionospheric plasma density during the ascending phase of SWARM A and B satellites, respectively. Each column, arranged from top to bottom, displays the latitudinal profile of N_e in the Asia, Africa, and America regions. In each panel, N_e index for the 22nd, 23rd, 24th, and 25th March are superimposed in blue, orange, green, and red colors, respectively. The data for Asia, Africa, and America are obtained by selecting the satellite orbit closest to longitudes 90°, 10°, and -90°, orderly.

Observations from SWARM A show rapid density fluctuations in the Asian sector at high latitudes on the day of the storm (March-23). The following day, a significant decrease in electron density is observed when the crests of the EIA become indiscernible, while a slight enhancement is observed at the trough. The African region shows a decrease in N_e, approximately 70 x $10^4 cm^{-3}$, on the day of the storm at the crest of the EIA. In the American longitude, as depicted by SWARM A during the ascending flight, there is a rise in plasma density at both low and mid-latitudes on the next day (24th March). The SWARM B, depicted in the right column of Figure 5, crossed the equator in the morning (LT~10.5) during the ascending phase. In the Asian sector, an enhancement (reduction) is observed on 24th March at the trough (crest) of the EIA, indicating an equatorward migration of ionospheric plasma density on the day after the storm. A similar trend, though with lesser intensity, is observed in the African region. In the American sector, an increase in plasma density at mid-latitudes is observed on March 25th, 2023. Figure 6, with left and right columns representing the same parameters as in Figure 5, depicts ionospheric plasma density during the descending phase of SWARMs A and B. The SWARM A data indicates a significant increase in electron density in the African region on March 24th, 2023, with double-peaked enhancements at 10° and 30° latitude in the northern hemisphere. A similar pattern is observed in the southern hemisphere of the American region. While SWARM B data reveals intense depletion in plasma density on the night-side during the descending phase on March 24th in the Asian region. In the African region, an increase in plasma

density on March 23rd is more pronounced in the northern crest of the EIA, with depletion at the respective trough. This indicates a poleward expansion of plasma on the day of the storm. The rapid oscillations in plasma density in the America region during the descending phase of SWARMs A and B correspond to the development of electron plasma bubbles.

3.5 Comparison with St. Patrick day storm

Figure 7, arranged from top to bottom, illustrates the IMF-Bz, SYM-H index, solar wind speed, AE index, and GEC from two days before the storm until the 7th day after the storm. In each panel, data for the storms on March-15 and March-23 are superimposed in blue and red, respectively. The IMF-Bz exhibits robust oscillations after the arrival of the CME depicting multiple north-south excursions during the March-15 case. However, the amplitude of these oscillations is comparatively lower, remaining predominantly southward over an extended period during the March-23 storm. The minimum value of IMF-Bz is -27.8 nT and -20.0 nT for the March-15 and March-23 cases, respectively. The solar wind speed increase to almost 110 km/s for the case March-15, whereas no such enhancement is observable, as CME strikes, for March-23 event. The SYM-H index starts to decrease earlier in the case of the March-15 storm compared to its counterpart, reaching a minimum value of -233 nT at 22:46 UT on the storm day. In contrast, for the March-23 storm, it reaches -170 nT at 05:21 UT on the March 24th, 2023. Both cases exhibit two main positive peaks, but the time span is longer during the March-23 event compared to March-15. Consequently, the degradation in GEC also initiates later for the March-23 case.

Figure 8 illustrates a comparative analysis of hemispheric REC across four longitudinal sectors for both the considered storms. Analogous to the GEC, the REC data for March-23 exhibits a temporal lag when contrasted with the March-15 data set. Diverging from the dynamics observed during the St. Patrick's Day storm, the Asian sector in March-23 displays an absence of a positive enhancement. The positive storm effect in the African sector is notably augmented during March-23, surpassing the March-15 counterpart by 0.05 GECU. The American sector manifests a relatively protracted duration of positive enhancement throughout the March-23 event. However, a pivotal distinction materializes in the Pacific region, wherein March-23 witnesses a positive storm enhancement of 0.35 GECU, concurrently compared with a negative storm effect of -0.38 GECU in the same region during the 2015 storm. Table 1 presents the UT and LT of occurrence of maximum negative peaks in REC at four longitudinal sectors for the considered storms.

The two magnetic storms of March 17, 2015 and March 23, 2023 beginning in the morning (~4:45 UT and ~06:00 UT) show important similarities for the variations of the GEC in the different sectors. The maximum of the GEC disturbance is observed first in Asia followed, respectively by Africa and America. The hemispheric REC decreases, indicative of an ionospheric negative storm, exhibit similar amplitudes from Asia towards America. For example, comparing March 17, 2015, with March 23, 2023, the REC decreases are as follows: Asia (0.38 GECU / 0.30 GECU), Africa (0.24 GECU / 0.20 GECU), and America (0.17 GECU / 0.17 GECU). For the case of 17 March 2015 there is a decrease (of 0.39 GECU) in the hemispheric REC for the Pacific region while no such trend is observed for the magnetic storm of 23 March 2023. The time delay between the onset of the magnetic storm and the maximum decrease in hemispheric REC in Asia is of the same order of magnitude, with 28 hours for the storm on March 17, 2015, and 30 hours for the storm on March 23, 2023. For the storm of March 17, 2015, the corresponding maximum decrease in the REC occurred at time spaced of 5-7 hours apart: 04.00 UT (Pacific), 09.00 UT (Asia), 15.00 UT (Africa), 22.30 UT (America). For the storm of March 23, 2023, the maximum decay in the REC of the hemisphere occurring in Africa at 13.30 UT, occurs one hour later than Asia at 12.00UT. Note that in the Europe Africa sector there is the propagation of a large scale travelling ionospheric disturbance (LSTID) during the case of March-2023 and the depletion of the REC at mid-latitudes may be associated to it (Kishore & Kumar, 2023)

To compare the intensity of super-fountain, we present in Fig. 9 the latitudinal distribution of GIM-TEC – on the day before (blue), storm day (red), two days after the storm (yellow and purple) – in the American sector (-70^{o}) at 23:15UT during the March-2023 (left) and March-2015 (right), respectively. The solar radio flux is high in March 2023 (157.53 sfu) as compared to March 2015 (126.89 sfu) which resulted in a stronger EIA. It can be seen that there is about 27TECU (48%) enhancement on the day after the storm (18th of March) at both crest of EIA during the March-15 storm. However, a hemispheric asymmetry is observed across the crest of EIA for the March-23 event having about 18TECU (19%) increase in the northern crest of EIA whereas it is 35TECU (35%) in southern counterpart (Nava et al., 2015; Tahir et al., 2024). Figures 10 (a and b) show the thermospheric O/N_2 ratios, as obtained by the Global Ultraviolet Imager (GUVI) on board the TIMED satellite, for the March-23 and March-15 cases, respectively. For the former case, the data is available only for the southern hemisphere. The UT and LT of equatorial crossing are indicated at the top of each panel. On March 23 and 24, there is a significant decrease in O/N_2 in the polar regions compared to March 22, the day before the storm. However, there is an asymmetric trend

in thermospheric variations at low- and mid-latitudes. The American low- and mid-latitudes show a relatively greater enhancement compared to the Asian counterpart, where even a decrease is observed. For the March 15 storm, the O/N_2 ratio increases mainly around the magnetic equator on March 17 and 18, with a more pronounced enhancement in the American region compared to the Asia (Fig. 10b). Astayeva et al. (2020) also reported similar hemispheric asymmetries during the August 2018 geomagnetic storm. The hemispheric asymmetry at high-latitudes can be attributed to several factors, including asymmetric energy inputs, the timing of the storm's onset, and seasonal effects. Additionally, the inherent north-south asymmetries in the geomagnetic field contribute to differences in the coupling between the magnetosphere, ionosphere, and thermosphere across the two hemispheres (Laundal et al., 2017).

4. Discussion

A detailed analysis of solar wind, geomagnetic parameters, and ionospheric behavior during the distinct storms on March-15 and March-23, has yielded valuable insights into the dynamic interplay of space weather phenomena. In this section, we explore the implications, on ionosphere, of our observations by investigating the variations in the IMF components, SYM-H index, and GEC. Through a comparison of these two events, our objective is to elucidate the underlying physical mechanisms that control space weather disturbances and their subsequent effects on Earth's ionospheric conditions.

The geomagnetic activity started on 23rd March around 0600 UT when the SYM-H index began to decrease (<0). There is a long, but relatively weak, compression phase (from 04:45 UT to 10:50 UT), which is followed by the main phase. Figure 1 shows several periods of energy transfer, as depicted by the AE magnetic index, during the main and recovery phases of the considered storm. The first AE maximum (EI; 1310 nT) occurs around 11:15UT; a second momentary one (EII; 1413 nT) around 1420 UT; third (EIII; 2609 nT) at 21:00UT; and the fourth maximum of the AE index (EIV; >1922 nT) has been found at 0700UT on 24th March. On 23rd March, the GEC exhibits two significant enhancements; one at 1400 UT (several hours after EI) and at 23:45 UT (several hours after EIII) and a smaller increase later at 07:00 UT on 24th March (see Figure 2, top panel).

The impact of the first input (EI; AE = 1310 nT) manifests as a positive storm effect, predominantly affecting the African sector, with minimal influence on other regions. Conversely, the effects of EII are deemed insignificant due to its brief and transient nature. The response to the third input (EIII;

AE = 2609 nT) manifests as a positive storm effect in the American and Pacific sectors. The observed third peak in GEC is mainly caused by the positive storm in the American sector (with a minor contribution from Africa) and is related to the input energy EIV (AE > 1922 nT, at 0700UT). Subsequently, negative storm effects are evident in all longitudinal sectors, beginning with Asia and extending to Africa, the Pacific, and finally, America, as illustrated by hemispheric REC data (Figure 2). The most pronounced negative storm effect is observed in the Asian sector. This observation aligns well with simulations by Fuller-Rowell et al. (1994), which suggest that the most substantial impact during geomagnetic storms occurs in the region situated on the nightside at the storm's onset, with the opposite being true on the day-side. When the storm initiated at 0445 UT, the Asian was on the day-side (around 12:00 LT) and hence the disturbance during the main phase is less noticeable in this sector.

To further examine the contribution of different latitudes and existence of north-south asymmetry (Paul et al., 2024), we analyze the low- and mid-latitudes of each hemisphere (Figures 3 and 4). In correspondence with the initial peak in GEC, primarily attributed to the African sector around local time 12:00, notable contributions have originated from the mid-latitudes of that sector. Specifically, the contributions are 0.06 GECU and 0.04 GECU, respectively for the northern and southern hemispheric regions of the mentioned sector. This enhancement is also evident in the plasma density data of SWARM B (Figure 6), which indicates a strong increase of plasma density at mid-latitude with a reduction at trough of EIA. Such trend is a signature of the super-fountain effect at low-latitudes, evident by a prominent depletion observed over the magnetic equator (Balan et al., 2018). In this case low-latitude plasma particles are lifted to much higher altitudes before they can diffuse downward, by the pressure gradient and gravity, along the magnetic field lines. Initially, it was suggested that this effect arises from strong eastward prompt penetration electric fields (PPEF) (Kelley et al., 2004). However, subsequent modeling studies have indicated that penetrating electric fields are not the only drivers of such phenomena (Balan et al., 2009). Indeed, the significant positive enhancement was explained by considering the combined effects of robust PPEF and equatorward thermospheric winds during storm-time conditions (e.g., Balan et al., 2011, Lu et al., 2012, Tsurutani et al., 2004). The low-latitudes and southern mid-latitudes region of America and Pacific sectors contributed equally to the 2nd peak of GEC, while the northern mid-latitudes showed no such contribution to this peak. This enhancement in the American low and mid regions is also illustrated by SWARM B during the descending phase, accompanied by a sudden reduction at the geomagnetic equator (Figure 6). During this timeframe, America and Pacific regions were on the evening and day-

side, respectively. Consequently, it suggests the presence of eastward PPEF as a contributing factor. The third positive storm effect on 24th March is primarily contributed by northern low-latitudes (Africa and America) and southern low-latitudes (America). While, the mid-latitude regions make no contribution to this positive increase. The positive increase is further supported by the observations of topside ionospheric plasma density by the SWARM A and B satellites. Moreover, during the descending phase, SWARM A reported an enhancement in the region of the EIA crest, accompanied by a significant reduction at the trough in the American region. Note that during this positive storm period the American section was on local nightside. The mechanism behind post-midnight enhancements in the electron density remains elusive and still remains to be a topic of future investigation. In this regard, Liu et al. (2013) emphasized the significant role of the westward electric field in shaping these enhancements in the ionospheric F layer over low-latitudes. Additionally, simulations conducted by Le et al. (2014) highlighted that the downward **E** × **B** plasma drift, induced by a westward electric field at night, serves as the primary driving force for the observed nighttime enhancement. They further noted that a delayed westward electric field can lead to a substantial post-midnight increase over the low-latitudes. Despite these findings, there is still a lack of observational support from the equatorial region. In this regard, Jiang et al. (2016) proposed the essential role of vertical **E** × **B** drift, coupled with meridional wind, in instigating post-midnight electron density enhancements across equatorial and low-latitudes.

The hemispheric REC showed that the most severe negative effect took place in the Asia region. This finding holds true for the low and mid-latitudes of each hemisphere, except for the southern mid-latitude region, where the maximum negative effect is observed in the African sector. Several interesting facts can be seen from the analysis of negative storm effect on 24th March in the Asian region, e.g. there is no asymmetry in the onset and intensity at hemispheric counterparts. However, the intensity of the negative storm effect is higher at low-latitudes (-0.1 GECU) compared to mid-latitudes (-0.08 GECU). There exists a time delay of about 10 hours at low-latitudes as compared to corresponding mid-latitudes. Furthermore, no significant negative storm effects are observed in either longitudinal sector of the Pacific region. Interestingly, the American region responded towards the end of this effect, and it is noteworthy that the intensity is higher at mid-latitudes compared to low-latitudes, which contrasts with the observed pattern in the Asian region. During geomagnetic storms, high-latitude Joule heating induces temperature variations, resulting in upward winds and the upwelling of air from the lower thermosphere into the F region. Simultaneously, the temperature increase at high-latitudes creates a robust equatorward horizontal

pressure gradient, enhancing neutral winds that transport N_2-rich/O-depleted air to mid and low latitudes. This indicates that the substantial increase in N_2 at high latitudes causes O/N_2 depletion, which extends to mid-low latitudes as storms progress (Kil et al., 2013). Conversely, changes in thermospheric circulation induced by storms lead to the downward movement of air in lower latitudes adjacent to the high-latitude upwelling region. This downward movement of O-rich/N_2-depleted air contributes to an increase in O/N_2. The pattern of O/N_2 enhancement is further spread toward the equator through horizontal transport (Fuller-Rowell et al., 1994).

Let us now compare the results with the ionospheric disturbances as generated by the March-15 storm. Despite the similarity in the scenarios of the two considered storms, notable differences in ionospheric variations are apparent as depicted in Figures 7 and 8. Both storms exhibit two major positive peaks in GEC after the arrival of CME. However, the timing of these enhancements is significantly different, with the peaks appearing earlier in the case of the March-15 event. Consequently, the negative and recovery phases also started earlier for the case of March-15 as compared to March-23 counterpart. As a result of this difference in the time of occurrence of GEC peaks, corresponding longitudinal sectors have also showed differences (Figure 8). This illustrates the remarkable sensitivity of space weather phenomena on ionospheric dynamics. An asymmetry in the TEC enhancement during March-23 can also be observed, with it being more pronounced in the southern crest of the Equatorial Ionization Anomaly (EIA). Another main difference that we observed is the complete absence of negative storm effects in the Pacific longitudinal sector for March-23. During both of the considered storms, the most intense negative storm effects occur in the Asian region which is consistent with simulations of Fuller-Rowell et al., (1994). High-latitude Joule heating elevates the temperature of the upper atmosphere, initiating a global wind surge from both polar regions that extends toward low-latitudes. This wind surge exhibits a preference for the night sector and aligns with the longitude of the magnetic pole, with its characteristics dependent on the start time (UT) of the storm. Since the time of commencement for both cases is the same, i.e. Asia is on the night-side in both instances, leading to the most intense negative storm effect occurring in this longitude sector. However, a notable longitudinal difference is observed for the positive storm effect, which could be associated with a time difference in the variation of IMF-Bz and energy inputs as estimated by the AE index.

The thermospheric O/N_2 ratio exhibits a longitudinally asymmetric trend at low- and mid-latitudes during the March 2023 storm. The south American low- and mid-latitude regions show more

significant enhancement as compared to the Asian counterpart, where a decrease is observed (Fig. 10). This longitudinal asymmetry is also reflected in the TEC and super fountain effect, which were not evident in the March-15 case. In a recent study, Oyama et al. (2024) reported the largest disturbed thermospheric wind observed by a Fabry-Perot interferometer in Tromsø since 2009. Thus, the intense, and non-uniform, disturbed thermospheric winds contributed to the asymmetry observed in the TEC and super-fountain effect in the American region.

Conclusions

In conclusion, this study has delved into the dynamics of ionospheric disturbances during the March 2023 geomagnetic storm, unraveling noteworthy patterns and behaviors. Main findings of this work are summarized as following:

1. The GEC index exhibits two major and one minor positive storm effects during the March 2023 storm. The initial increase is observed in the African sector, while the second is contributed by the Pacific and American sectors. The third positive increase leads to an enhancement in the American sector on March 24th. The two initial positive enhancements on 23rd March 2023 are associated with dayside PPEF. However, the 3rd such increase is contributed by the American sector, which was on the nightside. This may be associated by westward penetrating electric fields.

2. A negative storm effect is observed in all longitude sectors during the recovery phase of the storm, except in the Pacific sector during the March 2023 storm. The negative phase is more intense at low-latitudes compared to mid-latitude counterparts.

3. Furthermore, it commenced earlier at mid-latitudes than at low-latitudes in respective longitudes, suggesting that thermospheric neutral winds may be the main source of the observed negative storm effect. Regarding the negative storm effects, they are nearly identical during both events (March-15 and March-23), with the Asia longitude being the most affected region.

4. However, the positive storm effects differ when compared to the St. Patrick's Day storm. The Pacific mid-latitude region exhibit no positive storm effect during the March-2023 storm. This disparity may be associated with temporal difference in the episodes of energy input to ionosphere (as indicated by AE index). During the March 2015 storm, IMF Bz made several northward excursions

during the main phase contrary to March-23 where IMF remained southward for long duration. This difference of Bz variation may also lead to longitudinal difference in positive storm effect.

5. On March 18th, both crests of the equatorial ionization anomaly (EIA) show a substantial 27 TECU (48%) enhancement. However, during the March-23 storm, a hemispheric asymmetry was observed: a 19% increase (18 TECU) in the northern crest compared to a 35% increase (35 TECU) in the southern counterpart.

6. The asymmetric enhancement of TEC at the crest of the equatorial ionization anomaly (during the March-23) may be attributed to the non-uniform planetary distribution of disturbed thermospheric winds.

Acknowledgments

This research was supported by the NASA Living with a Star Jack Eddy Postdoctoral Fellowship Program, administered by UCAR's Cooperative Programs for the Advancement of Earth System Science (CPAESS) under award #80NSSC22M0097[1], NASA grants 80NSSC21K1321, 80NSSC23K0410 and 80NSSC23M0193, and AFOSR grant FA9550-23-1-0614. The authors are thankful to the IGS Community for providing GNSS data, OMNI web data center (http://omniweb.gsfc.nasa.gov/) for making available solar indices. We are grateful to the European Space Agency for making available Swarm data (https://swarm-diss.eo.esa.int/#swarm/Level2daily/Entire%5Fmission%5Fdata). The authors are thankful to the TIMED/GUVI management team (http://guvitimed.jhuapl.edu/) for providing thermospheric O/N_2 data used in thes work.

519

520

521

522

523

524

525

526

527

528

529

530

531

532

533

534

535

536

537

538

539

540

541

542

543 # References

Afraimovich, E. L., Astafyeva, E. I., & Zhivetiev, I. V. (2006). Solar activity and global electron content. Doklady Earth Sciences, 409(2),921–924. https://doi.org/10.1134/s1028334x06060195

Astafyeva, E., Zakharenkova, I., & Förster, M. (2015, October). Ionospheric response to the 2015 St. Patrick's Day storm: A global multi-instrumental overview. Journal of Geophysical Research: Space Physics. American Geophysical Union (AGU). https://doi.org/10.1002/2015ja021629

Astafyeva, E., Bagiya, M. S., Förster, M., & Nishitani, N. (2020, March). Unprecedented Hemispheric Asymmetries During a Surprise Ionospheric Storm: A Game of Drivers. Journal of Geophysical Research: Space Physics. American Geophysical Union (AGU). https://doi.org/10.1029/2019ja027261

Balan, N., Shiokawa, K., Otsuka, Y., Watanabe, S., & Bailey, G. J. (2009). Super plasma fountain and equatorial ionization anomaly during penetration electric field. Journal of Geophysical Research: Space Physics. American Geophysical Union (AGU). https://doi.org/10.1029/2008ja013768

Balan, N., Yamamoto, M., Liu, J. Y., Otsuka, Y., Liu, H., & Lühr, H. (2011, July). New aspects of thermospheric and ionospheric storms revealed by CHAMP. Journal of Geophysical Research: Space Physics. American Geophysical Union (AGU). https://doi.org/10.1029/2010ja016399

Balan, N., Liu, L., & Le, H. (2018). A brief review of equatorial ionization anomaly and ionospheric irregularities. Earth and Planetary Physics. Earth and Planetary Physics. https://doi.org/10.26464/epp2018025

Fuller-Rowell, T. J., M. V. Codrescu, R. J. Moffett, and S. Quegan (1994), Response of the thermosphere and ionosphere and geomagnetic storms, J. Geophys. Res., 99, 3893–3914, doi:10.1029/93JA02015.

Heelis, R. A., & Maute, A. (2020). Challenges to Understanding the Earth's Ionosphere and Thermosphere. Journal of Geophysical Research: Space Physics. American Geophysical Union (AGU). https://doi.org/10.1029/2019ja027497

Kelley, M. C., Vlasov, M. N., Foster, J. C., & Coster, A. J. (2004, October). A quantitative explanation for the phenomenon known as storm-enhanced density. Geophysical Research Letters. American Geophysical Union (AGU). https://doi.org/10.1029/2004gl020875

Kishore, A., & Kumar, S. (2023). Large Scale Traveling Ionospheric Disturbances During Geomagnetic Storms of 17 March and 23 June 2015 in the Australian Region. Journal of Geophysical Research: Space Physics. American Geophysical Union (AGU). https://doi.org/10.1029/2023ja031740

Koga, D., Sobral, J. H. A., Gonzalez, W. D., Arruda, D. C. S., Abdu, M. A., de Castilho, V. M., et al. (2011). Electrodynamic coupling processes between the magnetosphere and the equatorial ionosphere duringa 5-day HILDCAA event. Journal of Atmospheric and Solar -Terrestrial Physics, 73(1), 148–155. https://doi.org/10.1016/j.jastp.2010.09.002

Laundal, K. M., Cnossen, I., Milan, S. E., Haaland, S. E., Coxon, J., Pedatella, N. M., Förster, M., & Reistad, J. P. (2017). North-south asymmetries in Earth magnetic field. Space Science Reviews, V., 206(1-4), 225–257. https://doi.org/10.1007/s11214-016-0273-0

Liu, B., Zhang, X., He, F., & Zong, Q. (2019). The Magnetic Local Time Distribution of Storm Geomagnetic Field Disturbance Under Different Conditions of Solar Wind and Interplanetary Magnetic Field. Journal of Geophysical Research: Space Physics. American Geophysical Union (AGU). https://doi.org/10.1029/2018ja026287

Lu, G., Goncharenko, L., Nicolls, M. J., Maute, A., Coster, A., & Paxton, L. J. (2012, August). Ionospheric and thermospheric variations associated with prompt penetration electric fields. Journal of Geophysical Research: Space Physics. American Geophysical Union (AGU). https://doi.org/10.1029/2012ja017769

Jiang, C., Chunhua, J., Chi, D., Guobin, Y., Jing, L., Peng, Z., Tatsuhiro, Y., et al. (2016). Latitudinal variation of the specific local time of postmidnight enhancement peaks in F layer electron density at low latitudes: A case study. Journal of Geophysical Research: Space Physics, 121, 3476–3483. https://doi.org/10.1002/2015JA022319

Kil, H., Lee, W. K., Shim, J., Paxton, L. J., & Zhang, Y. (2013). The effect of the 135.6 nm emission originated from the ionosphere on the TIMED/GUVI O/N ratio. Journal of Geophysical Research: Space Physics, 118(2), 859–865. https://doi.org/10.1029/2012JA018112

Materassi, M., Alberti, T., Migoya-Orué, Y., Radicella, S. M., & Consolini, G. (2023, February 17). Chaos and Predictability in Ionospheric Time Series. Entropy. MDPI AG. https://doi.org/10.3390/e25020368

Maurya, A. K., Venkatesham, K., Kumar, S., Singh, R., Tiwari, P., & Singh, A. K. (2018, August). Effects of St. Patrick's Day Geomagnetic Storm of March 2015 and of June 2015 on Low-Equatorial D Region Ionosphere. Journal of Geophysical Research: Space Physics. American Geophysical Union (AGU). https://doi.org/10.1029/2018ja025536

Mridula, N., Manju, G., Sijikumar, S., Kumar Pant, T., & Kumar Choudhary, R. (2022, December). On the significant impact of the 17 March 2015 St. Patrick's Day geomagnetic storm on the ionosphere over Indian region. Advances in Space Research. Elsevier BV. https://doi.org/10.1016/j.asr.2022.08.022

Nava, B., Rodríguez-Zuluaga, J., Alazo-Cuartas, K., Kashcheyev, A., Migoya-Orué, Y., Radicella, S. M., et al. (2016). Middle- and low-latitude ionosphere response to 2015 St. Patrick's Day geomagnetic storm. Journal of Geophysical Research: Space Physics, 121,3421–3438. https://doi.org/10.1002/2015JA022299

Le, H., Liu, L., Chen, Y., Zhang, H., & Wan, W. (2014). Modeling study of nighttime enhancements in F region electron density at low latitudes. Journal of Geophysical Research: Space Physics, 119, 6648–6656. https://doi.org/10.1002/2013JA019295

Liu, L., Chen, Y., Le, H., Ning, B., Wan, W., Liu, J., & Hu, L. (2013). A case study of postmidnight enhancement in F-layer electron density over Sanya of China. Journal of Geophysical Research: Space Physics, 118, 4640–4648. https://doi.org/10.1002/jgra.50422

Ogunsua, B. O., Laoye, J. A., Fuwape, I. A., & Rabiu, A. B. (2014, January 20). The comparative study of chaoticity and dynamical complexity of the low-latitude ionosphere, over Nigeria, during quiet and disturbed days. Nonlinear Processes in Geophysics. Copernicus GmbH. https://doi.org/10.5194/npg-21-127-2014

Oyama, S., Vanhamäki, H., Cai, L., Shinbori, A., Hosokawa, K., Sakanoi, T., et al. (2024). Thermospheric Wind Response to March 2023 Storm: Largest Wind Ever Observed With a

628 Fabry-Perot Interferometer in Tromsø, Norway Since 2009. Space Weather. American
629 Geophysical Union (AGU). https://doi.org/10.1029/2023sw003728

630 Olsen, N., et al. (2013), The Swarm Satellite Constellation Application and Research Facility (SCARF)
631 and Swarm data products, Earth Planets Space, 65, 1189–1200

632 Paul, K. S., Haralambous, H., & Oikonomou, C. (2024). Ionospheric response of the March 2023
633 geomagnetic storm over European latitudes. Advances in Space Research. Elsevier BV.
634 https://doi.org/10.1016/j.asr.2024.03.026

635 Tsurutani, B., Mannucci, A., Iijima, B., Abdu, M. A., Sobral, J. H. A., Gonzalez, W., et al. (2004,
636 August). Global dayside ionospheric uplift and enhancement associated with interplanetary
637 electric fields. Journal of Geophysical Research: Space Physics. American Geophysical Union
638 (AGU). https://doi.org/10.1029/2003ja010342

639 Tahir, A., Wu, F., Shah, M., Amory-Mazaudier, C., Jamjareegulgarn, P., Verhulst, T. G. W., & Ameen,
640 M. A. (2024). Multi-Instrument Observation of the Ionospheric Irregularities and Disturbances
641 during the 23–24 March 2023 Geomagnetic Storm. Remote Sensing. MDPI AG.
642 https://doi.org/10.3390/rs16091594

643 Unnikrishnan, K., Saito, A., & Fukao, S. (2006, June). Differences in magnetic storm and quiet
644 ionospheric deterministic chaotic behavior: GPS total electron content analyses. Journal of
645 Geophysical Research: Space Physics. American Geophysical Union (AGU).
646 https://doi.org/10.1029/2005ja011311

647 Wu, C.-C., Liou, K., Lepping, R. P., Hutting, L., Plunkett, S., Howard, R. A., & Socker, D. (2016). The
648 first super geomagnetic storm of solar cycle 24: "The St. Patrick's day event (17 March 2015)."
649 Earth, Planets and Space. Springer Science and Business Media LLC.
650 https://doi.org/10.1186/s40623-016-0525-y

651 Younas, W., Amory-Mazaudier, C., Khan, M., & Fleury, R. (2020). Ionospheric and magnetic
652 signatures of a space weather event on 25–29 August 2018: CME and HSSWs. Journal of
653 Geophysical Research: Space Physics, 125(8), e2020JA027981.
654 https://doi.org/10.1029/2020ja027981

655 Yadav, S., Choudhary, R. K., Kumari, J., Sunda, S., Shreedevi, P. R., & Pant, Tarun. K. (2020, May).
656 Reverse Fountain and the Nighttime Enhancement in the Ionospheric Electron Density Over

the Equatorial Region: A Case Study. Journal of Geophysical Research: Space Physics. American Geophysical Union (AGU). https://doi.org/10.1029/2019ja027286

Table Captions

Table 1: The onset time of the storm and the peak reduction in hemispheric REC for the March 15 and March 23 storms.

Figure Captions

Figure 1: (From top to bottom) IMF-Bz in nT, solar wind speed in km/s, pressure in nPa, AE, and SYM-H index in nT from March 21 to March 29, 2023.

Figure 2: (Top) Difference in Global Electron Content (GEC) from March 21 to March 29, 2023. (Bottom) Difference in Regional Electron Content (REC) at four longitudinal sectors: Asia (blue), Africa (red), America (yellow), and Pacific (magenta) from March 21 to March 29, 2023.

Figure 3: Difference in REC at low (top) and mid (bottom) latitude sectors from March 21 to March 29, 2023. The left panel corresponds to the northern region, and the right panel presents the southern counterpart. On each panel, Asia, Africa, America, and Pacific are represented, respectively by blue, red, yellow, and magenta.

Figure 4: (a) The ΔvTEC at fixed longitudes of the eastern hemisphere during March 21 to March 29, 2023, from top to bottom: 180, 135, 90, 45, respectively. (b) Similar to Figure 4a but for the western hemisphere.

Figure 5: Plasma density measurement from SWARM A (left) and SWARM B (right) satellites during the ascending phase at three longitudinal regions, from top to bottom: Asia, Africa, and America, respectively. On each panel, data for March 22, 23, 24, and 25 are superimposed in blue, yellow, green, and red color lines, orderly.

Figure 6: Similar to Figure 5 but during the descending flight of SWARM satellites.

Figure 7: From the top to bottom, a comparison of IMF-Bz, SYM-H index, solar wind speed, AE index and GEC variations during the March 2015 (red) and March 2023 (black) storms.

Figure 8: A comparison of REC variation during the March 2013 (in black) and March 2015 (in red) storms in Asia, Africa, America, and Pacific regions, respectively.

Figure 9: A comparison of super-fountain effect in the American region during the March 2015 (right) and March 2023 (left) storms. Each panel depicts the latitudinal variation of GIM-TEC on the day before (blue), storm day (red), two days after (yellow and purple) the storm, respectively.

Figure 10: (a) Thermospheric O/N_2 measured by GUVI on board TIMED satellite on 22^{nd} (bottom left), 23^{rd} (bottom right), 24^{th} (top left), and 25^{th} (top right) March 2023, respectively. (b) Similar to Fig. 10a but for 16^{th}, 17^{th}, 18^{th} and 19^{th} of the March 2015, respectively.

735

736

737

738

739

740

741

742

743

744

745

746

747

748

749

750

751

752

753 **Table 1**

754

755

756

Case	March-15	March-23
Beginning of disturbance (t_o)	~17-March-2015 ~04. 45 Time of increase AE: 06:00	~23-March-2023 ~06:00 Time of increase of AE: 08:00
Maximum decrease in Hemispheric REC for Pacific	18 Mar-2015 04:00:00 (~21:00 LT) Delay: 23 hours 0.39GECU	No Decrease
Maximum decrease in Hemispheric REC for Asia	18-Mar-2015 09:00:00 (~16:00 LT) Delay: 28 hours 0.38GECU	24-Mar-2023 12:00:00 (~19:00LT) Delay: 30 hours 0.30GECU
Maximum decrease in Hemispheric REC for Africa	18-Mar-2015 15:15:00 (~15:15 LT) Delay: 34 hours 0.24GECU	24-Mar-2023 13:30:00 (~13:30 LT) Delay: 31 hours 30 minutes 0.20GECU
Maximum decrease in Hemispheric REC for America	18-Mar-2015 22:30:00 (~17:30 LT) Delay: 41 hours 30 minutes 0.17GECU	24-Mar-2023 19:15:00 (~14:15 LT) Delay: 33 hours 0.17GECU

Figure 1

Click here to access/download;Figure;Figure_1.pdf

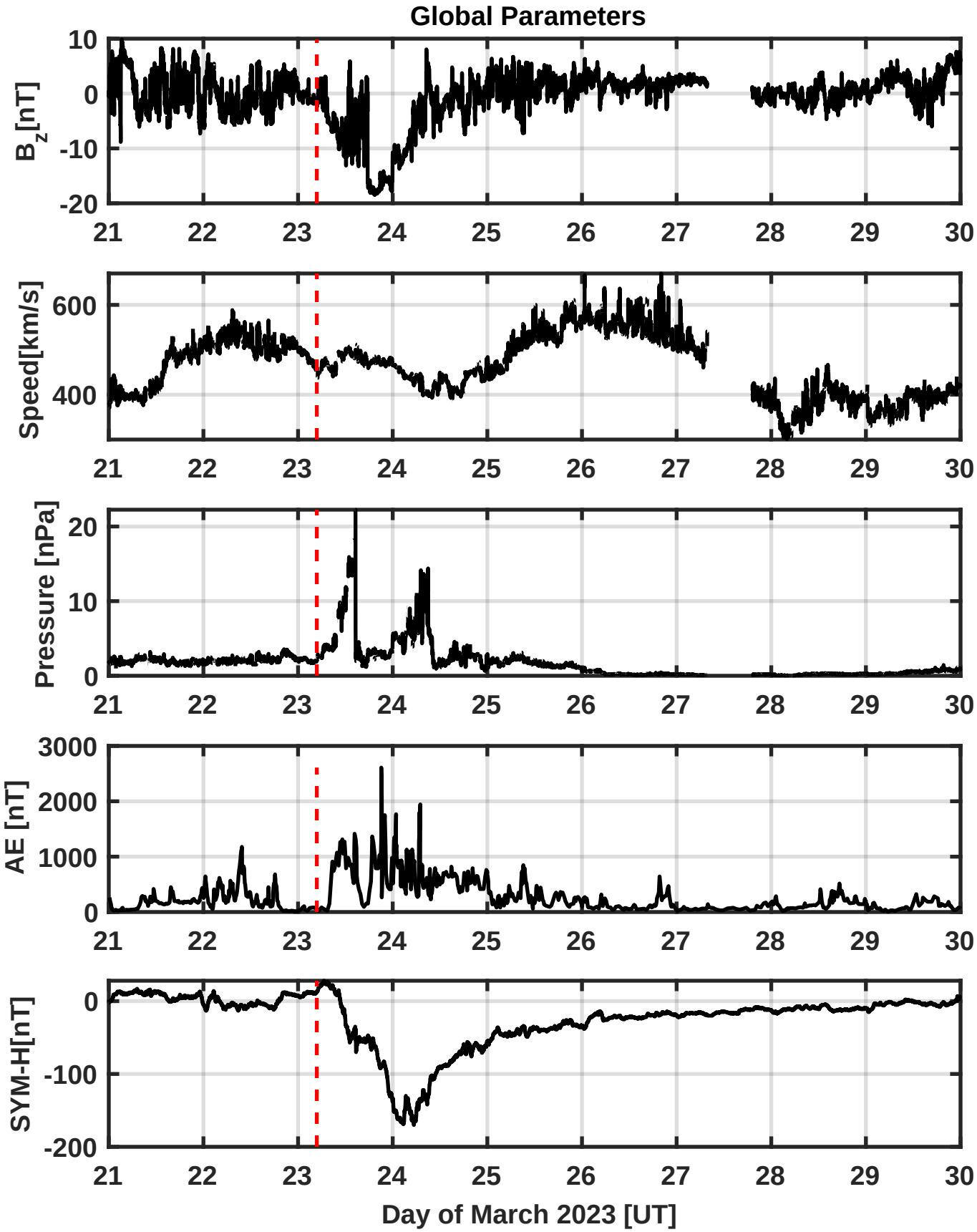

Figure 2

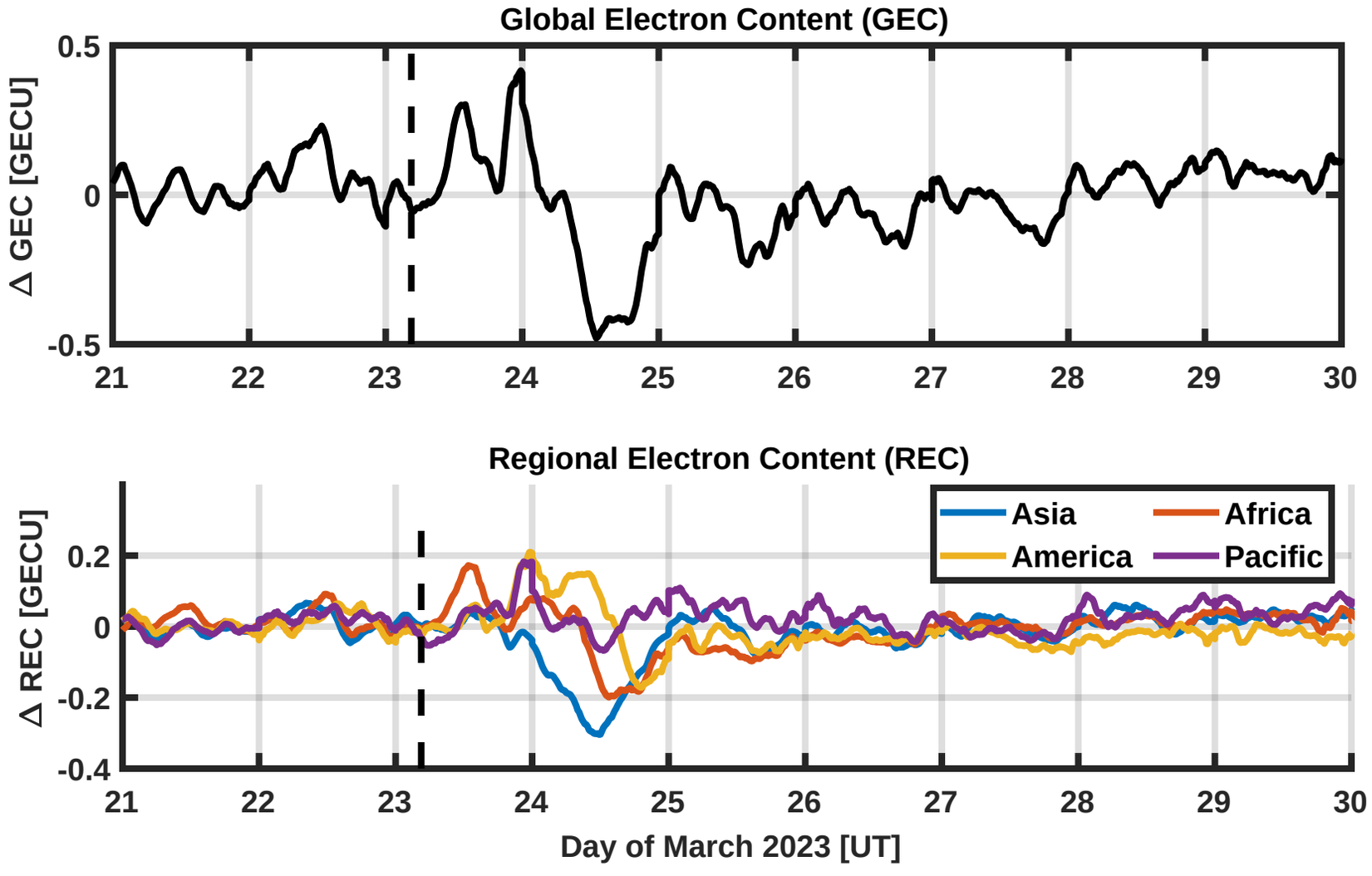

Figure 3

Click here to access/download;Figure;Figure_3.jpg

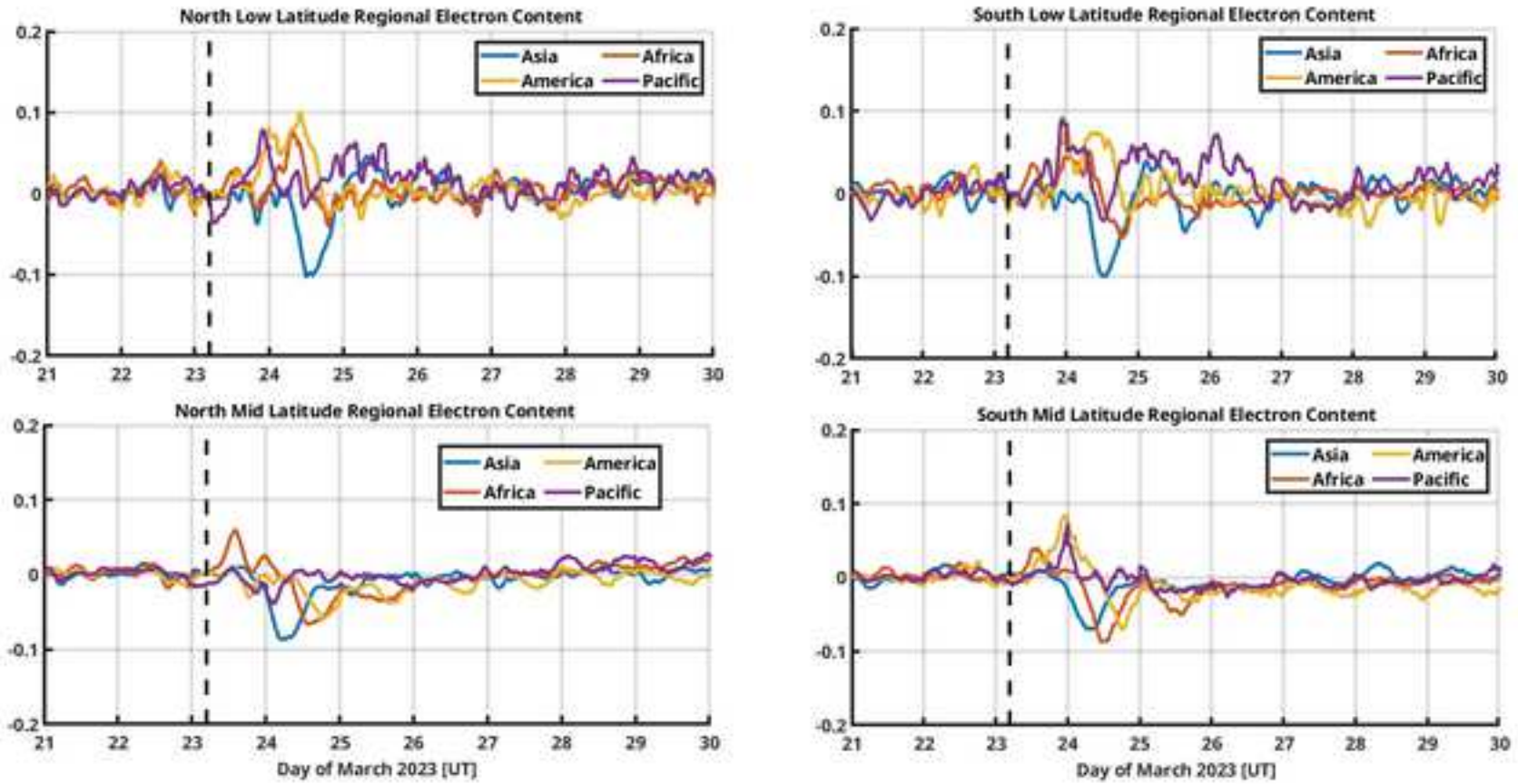

Figure 4

Click here to access/download;Figure;Figure_4.jpg

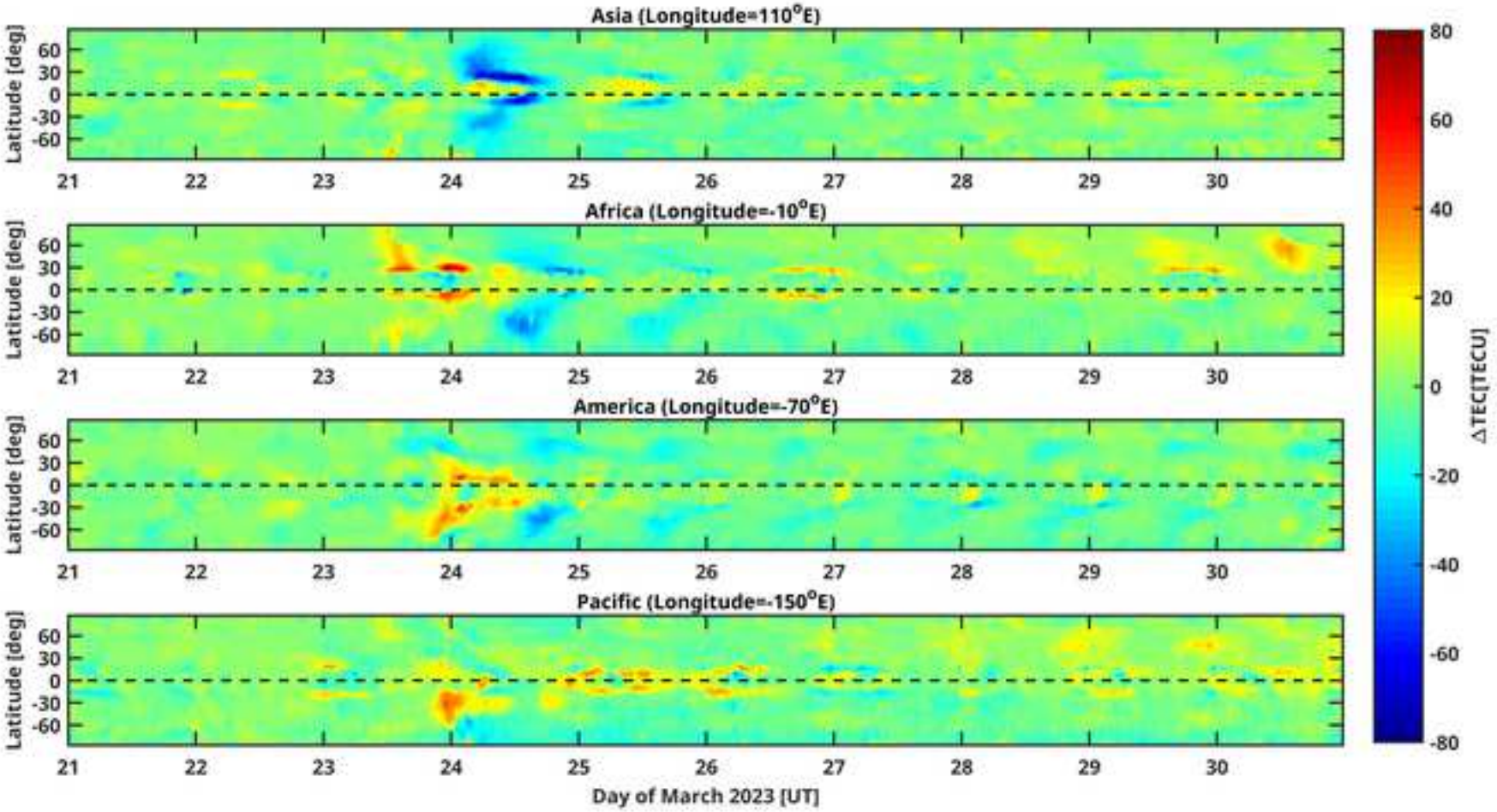

Figure 5

Click here to access/download;Figure;Figure_5.jpg

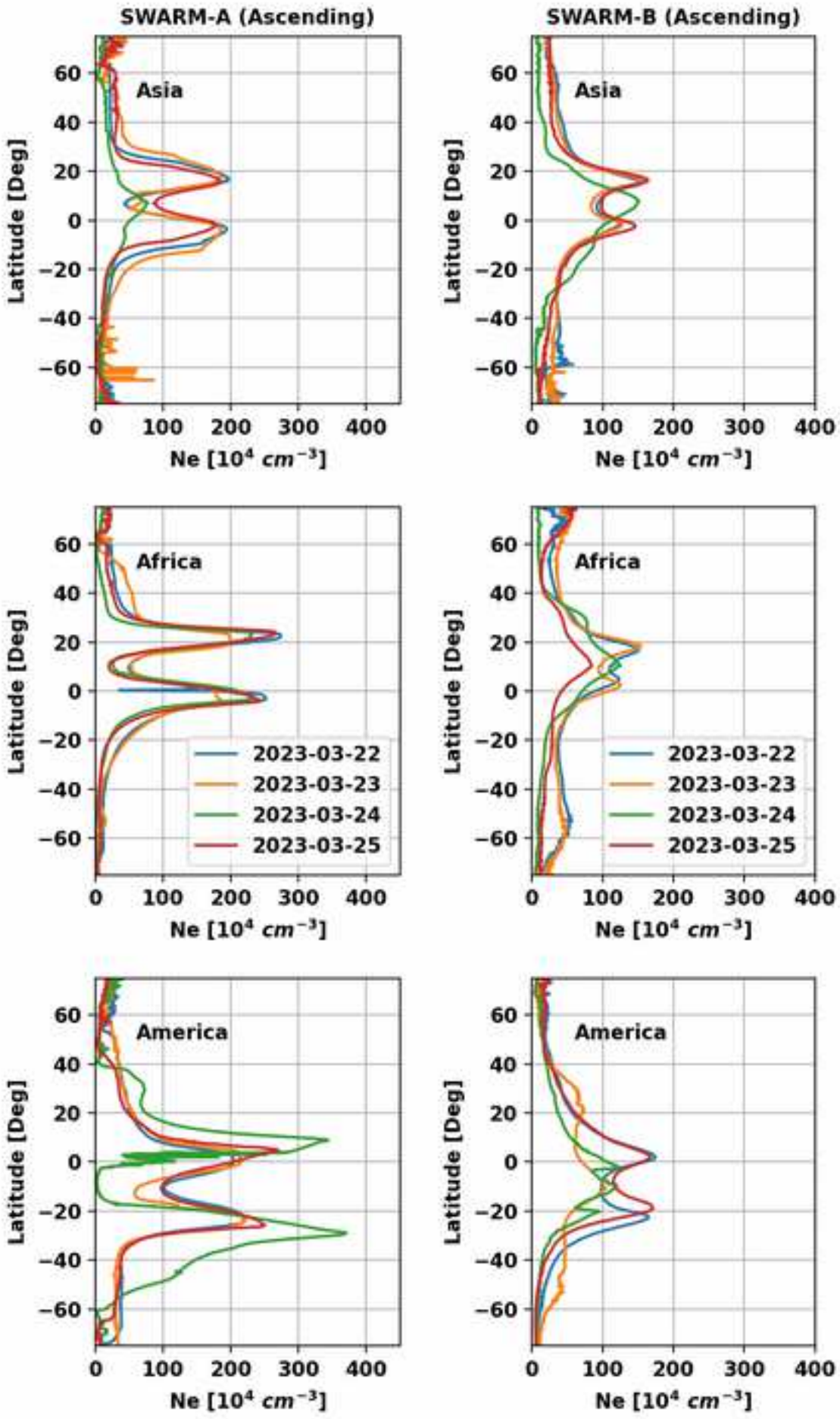

Figure 6

Click here to access/download;Figure;Figure_6.jpg

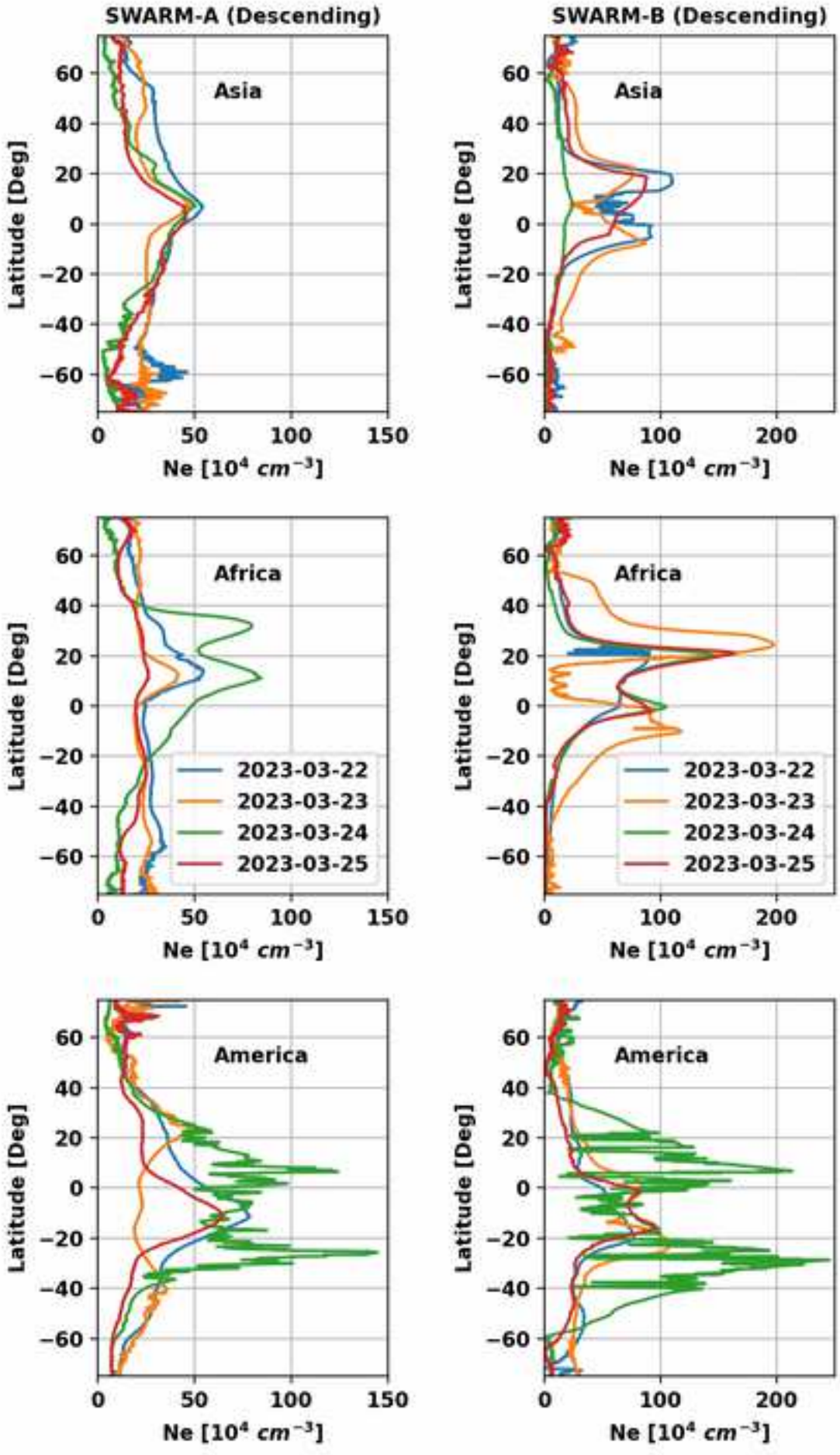

Figure 7

Click here to access/download;Figure;Figure_7.eps

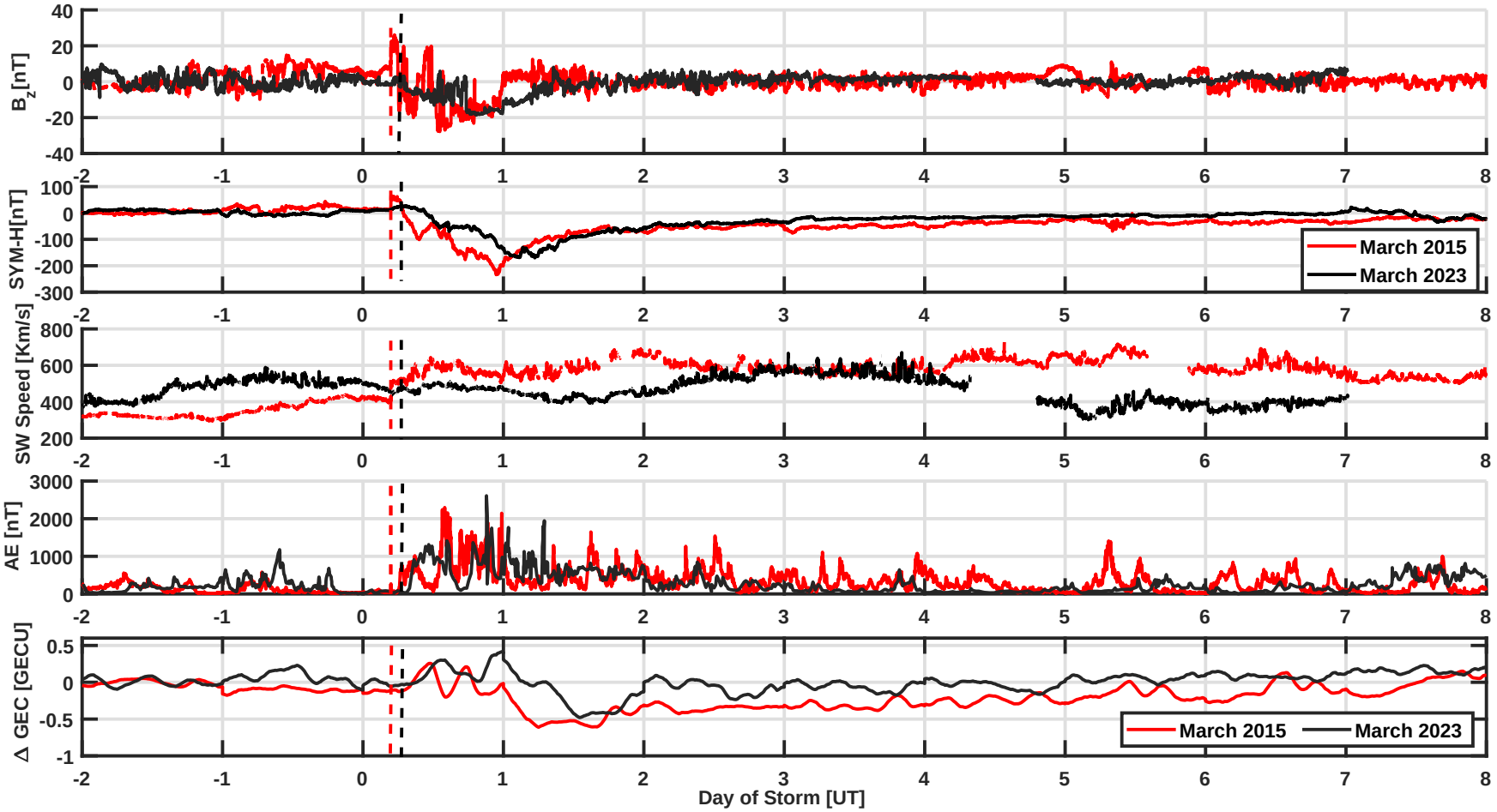

Figure 8

Click here to access/download;Figure;Figure_8.jpg

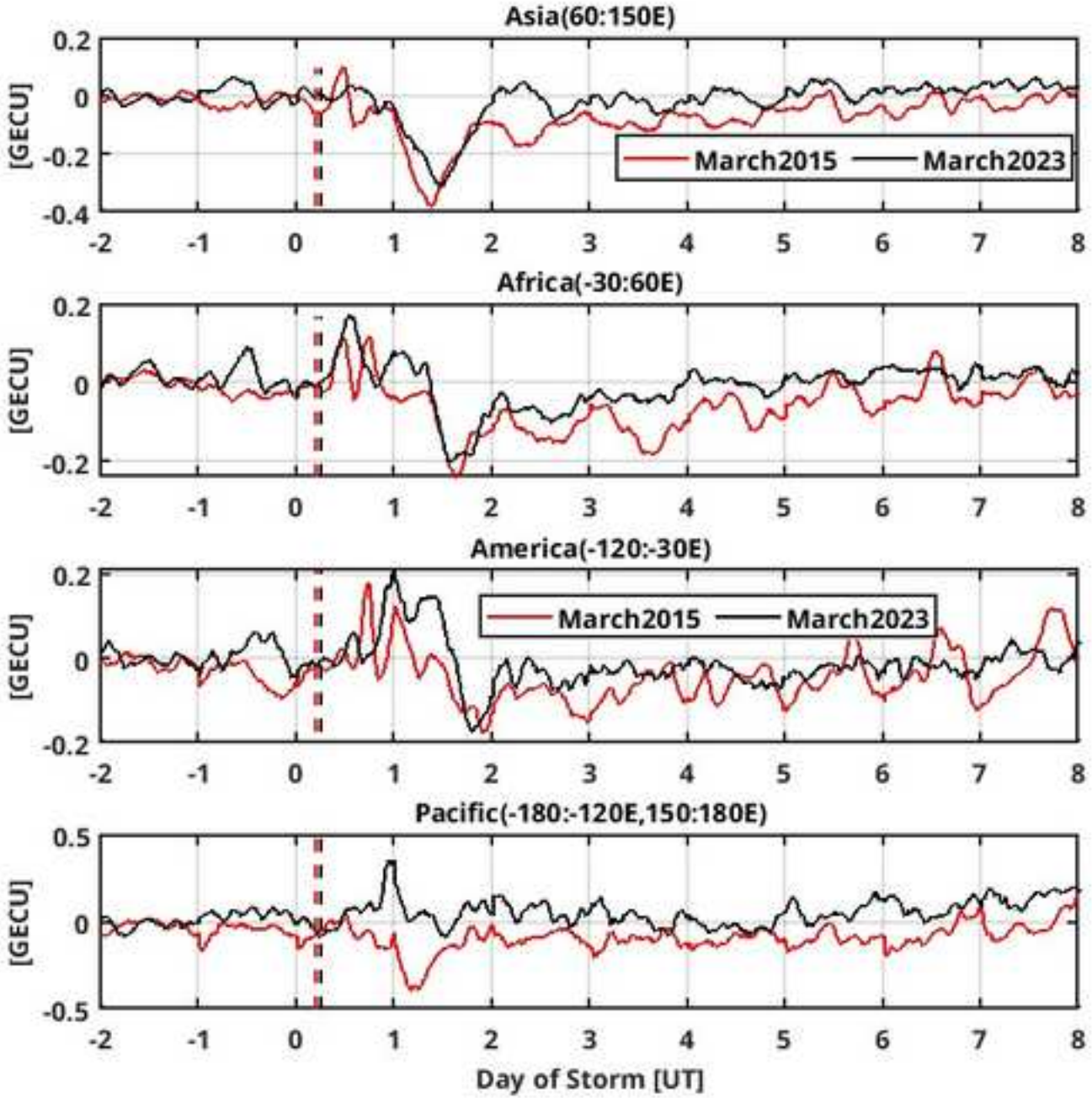

Figure 9

Click here to access/download;Figure;Figure_9.jpg

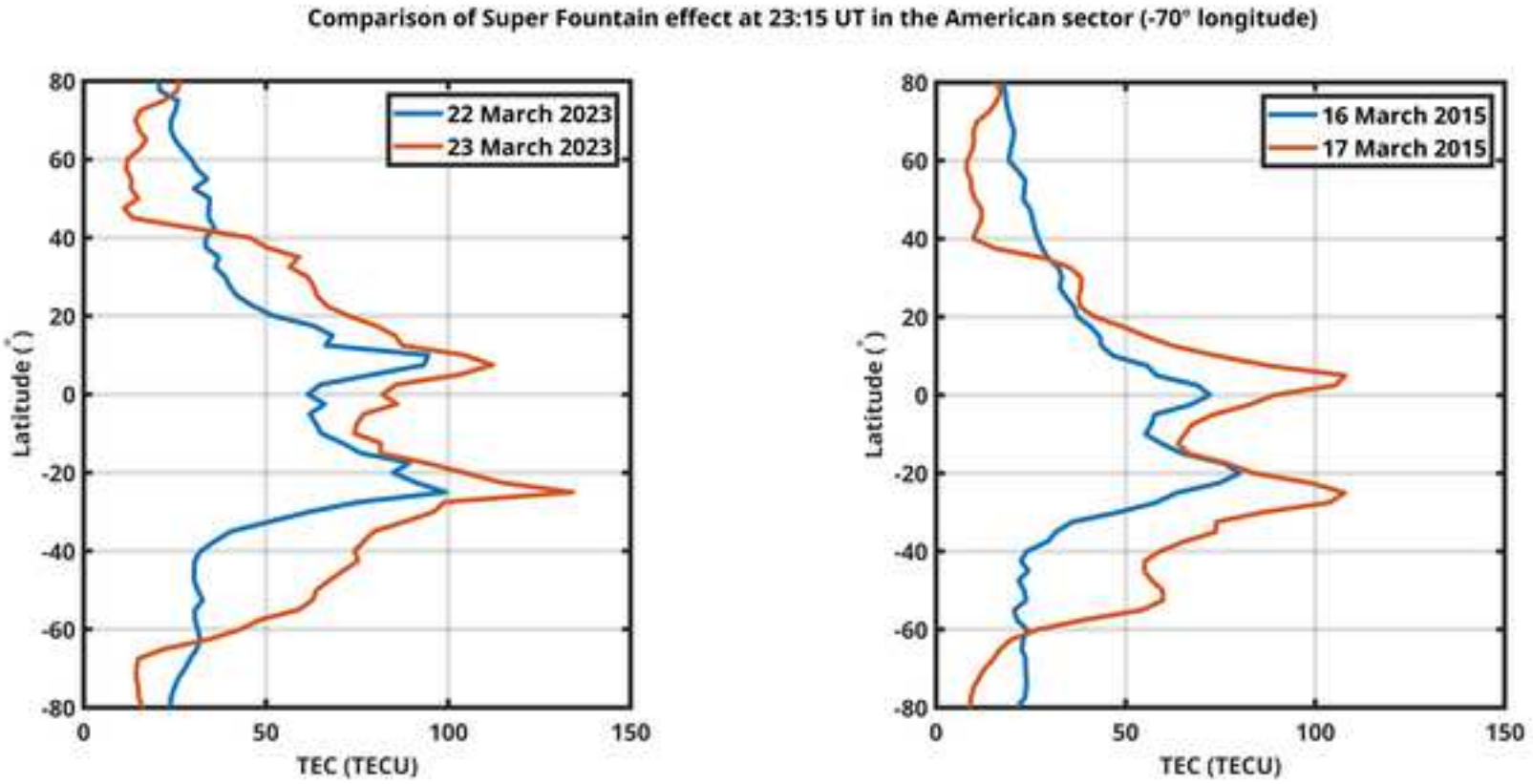

Figure 10a

Click here to access/download;Figure;Figure_10a.pdf

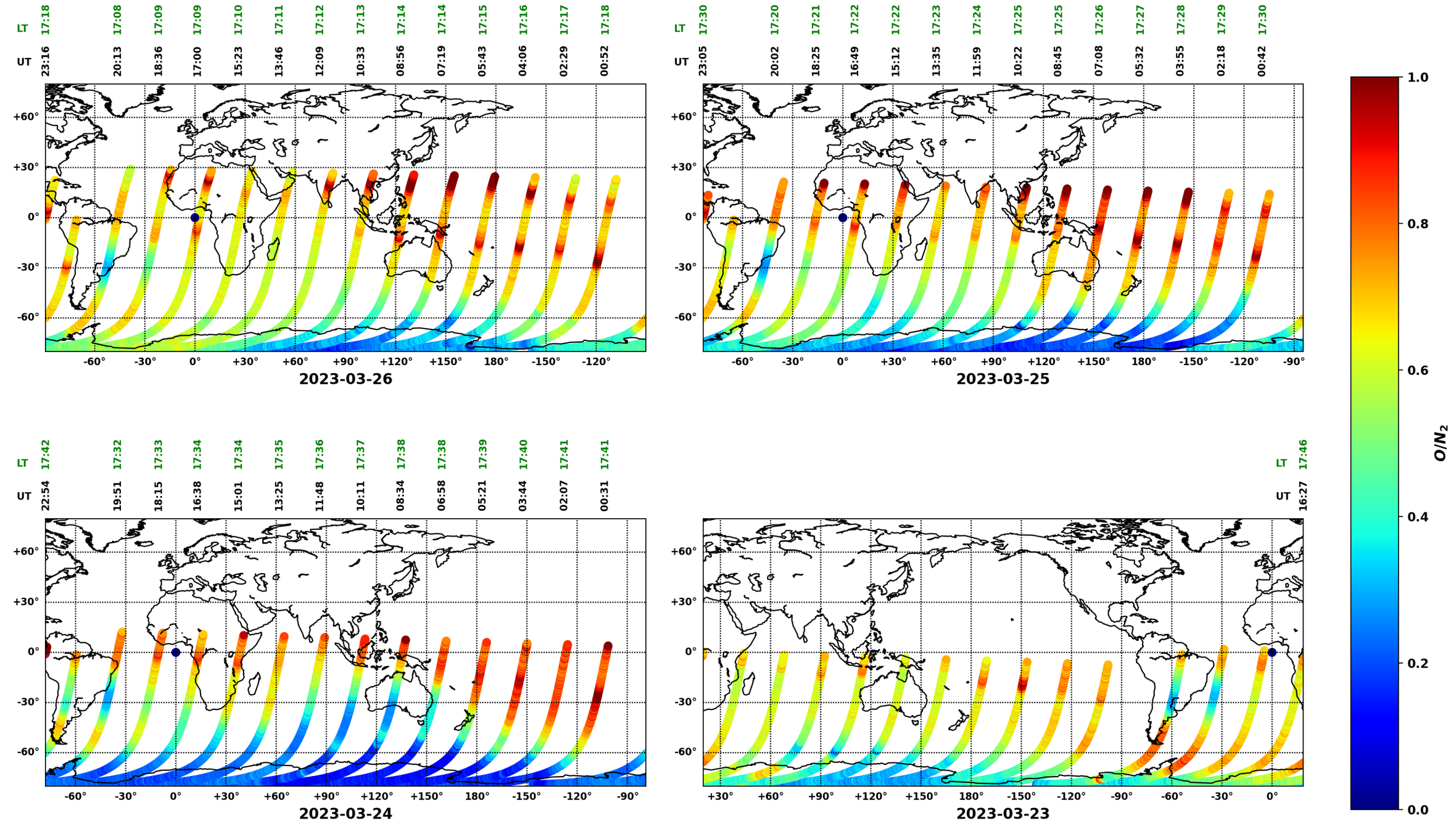

Figure 10b

Click here to access/download;Figure;Figure_10b.pdf